Supplementary materials - Forest disturbances intensify land surface warming across Europe

Authors

Yang Su [a, b, c], Yidi Xu [b], Xianglin Zhang [c], David Makowski [d], Agnes Pellissier-tanon [b], Saverio Francini [e], Tianqi Shi [b], Ke Yu [b], Siyu Liu [f], Haotian Chen [g, c], Haoruo Li [h], Jinfeng Chang [i], Songchao Chen [i], Chaohui Yin [j], Nikola Besic [k, l], Martin Brandt [f], Alba Viana-Soto [m], Katja Kowalski [n], Cornelius Senf [m], Alexandre d'Aspremont [a], Philippe Ciais [b]

Affiliations

[a] CNRS & Département d'Informatique, École Normale Supérieure – PSL, 45 Rue d'Ulm, 75005 Paris, France

[b] Laboratoire des Sciences du Climat et de l'Environnement, CEA CNRS UVSQ Orme des Merisiers, 91190 Gif-sur-Yvette, France

[c] Université Paris-Saclay, AgroParisTech, INRAE, UMR ECOSYS, 91120 Palaiseau, France

[d] Université Paris-Saclay, AgroParisTech, INRAE, Unit Applied Mathematics and Computer Science (MIA 518), 91120 Palaiseau, France

[e] Department of Science and Technology of Agriculture and Environment (DISTAL), University of Bologna, 40126 Bologna, Italy

[f] Department of Geosciences and Natural Resource Management, University of Copenhagen, Copenhagen, Denmark

[g] Institute of Crop Sciences, Chinese Academy of Agricultural Sciences / Key Laboratory of Crop Physiology and Ecology, Ministry of Agriculture and Rural Affairs of China, 100081 Beijing, China

[h] State Key Laboratory of Efficient Utilization of Arable Land in China，the Institute of Agricultural Resources and Regional Planning, Chinese Academy of Agricultural Sciences, 100081 Beijing, PR China

[i] College of Environmental and Resource Sciences, Zhejiang University, 310058 Hangzhou, China

[j] School of Resource and Environment, Henan Agricultural University, 450046 Zhengzhou, China

[k] Université de Lorraine, Géodata Paris, IGN, LIF, F-54000, Nancy, France

[l] Université Gustave Eiffel, Géodata Paris, IGN, Laboratoire d'inventaire forestier, F-54000, Nancy, France

[m] School of Life Sciences, Earth Observation for Ecosystem Management, Technical University of Munich, Freising, Germany

[n] Geography Department, Humboldt-Universität zu Berlin, Berlin, Germany

Corresponding Author

Yang Su	yang.su@ens.fr	+33 1 89 10 07 67	École Normale Supérieure – PSL
Yidi Xu	yidi.xu@lsce.fr	+33 6 71 68 25 78	LSCE

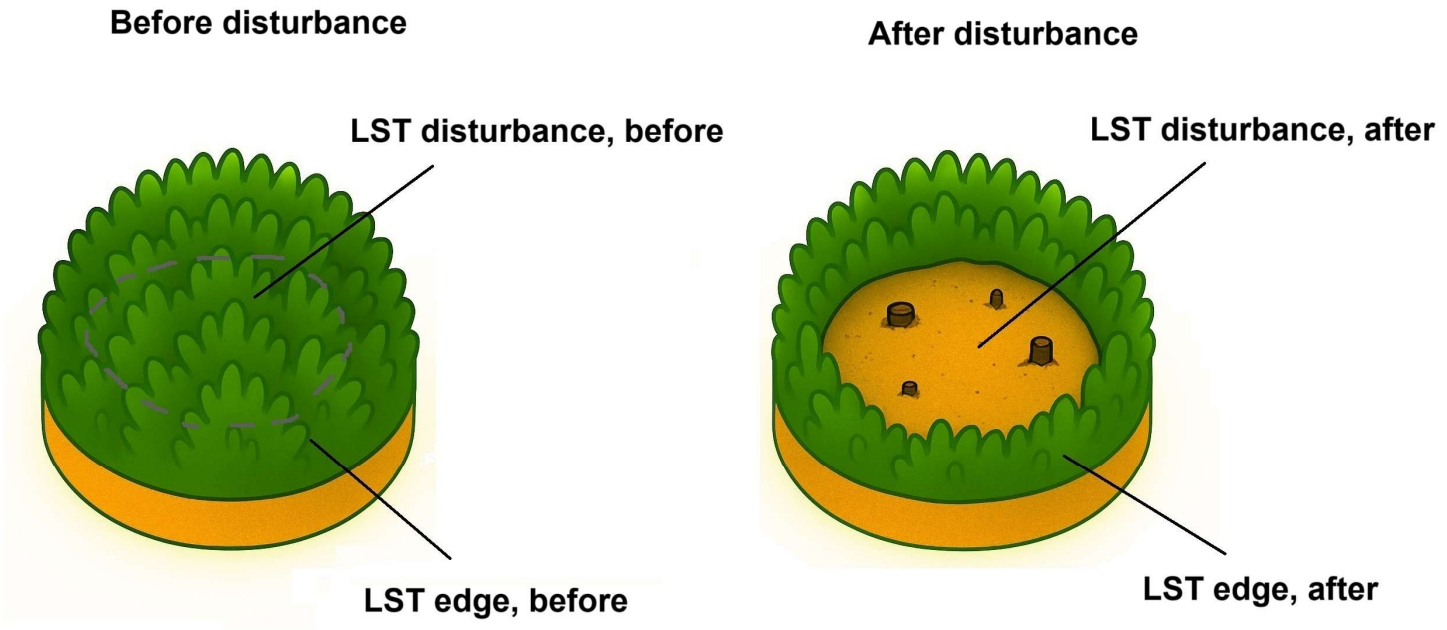

$$\text{LST anomaly} = (\text{LST disturbance, after} - \text{LST edge, after}) - (\text{LST disturbance, before} - \text{LST edge, before})$$

Supplementary Figure 1 | Conceptual illustration of disturbance-induced LST anomalies. Schematic showing land surface temperature (LST) conditions in disturbed areas and their surrounding forest edges before (left) and after (right) disturbance. Disturbance-induced LST anomaly is calculated as the change in LST anomalies between disturbed and edge pixels after disturbance, relative to the pre-disturbance baseline. This approach isolates disturbance effects from background climatic variability.

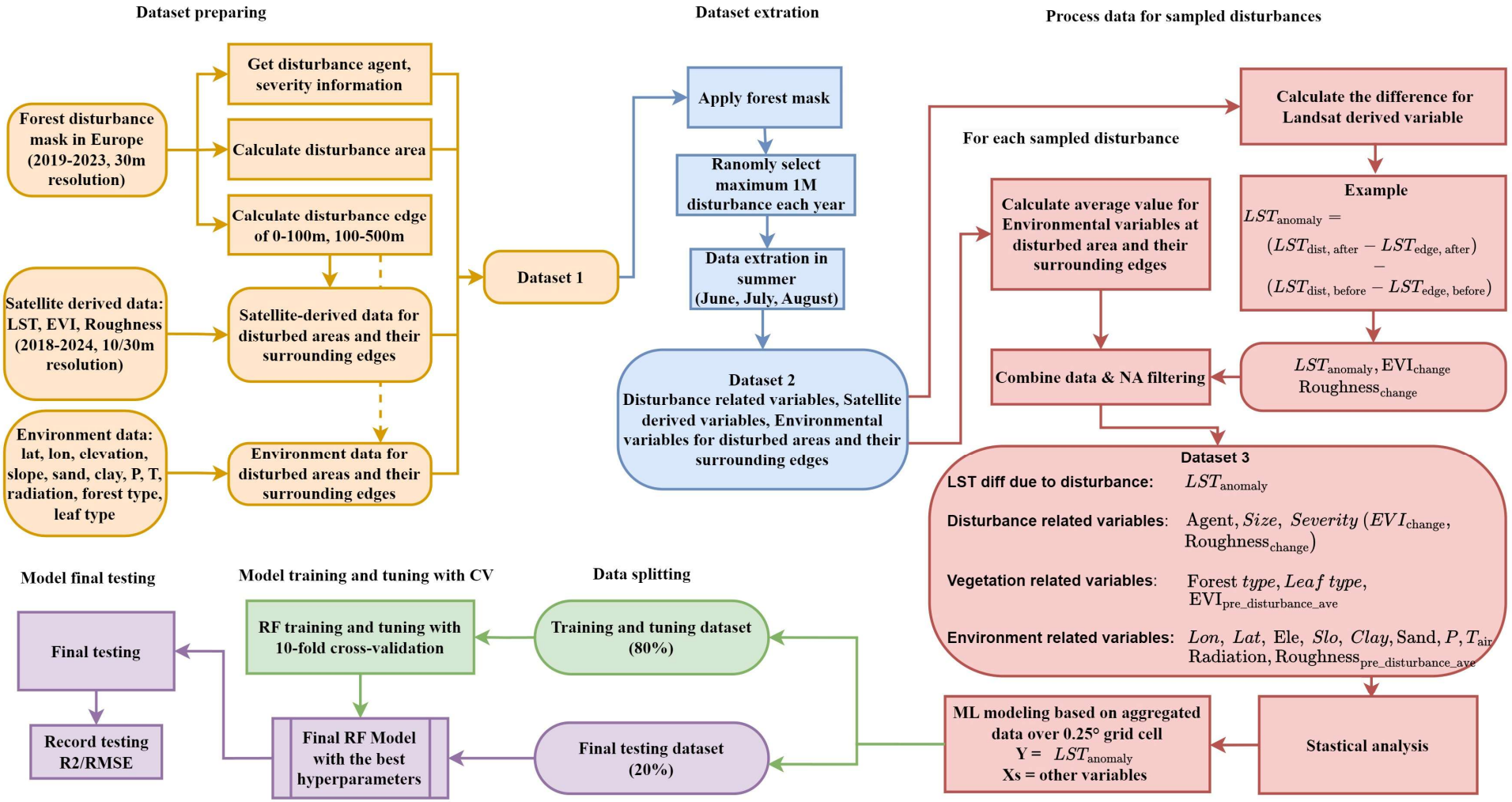

Supplementary Figure 2 | Workflow for analyzing the instantaneous LST response to forest disturbance. Flowchart showing the preparation of disturbance, Landsat, and environmental datasets, the extraction of variables for disturbed areas and their forest edges (0–100 m, 100–500 m), and the calculation of disturbance-induced anomalies (e.g., $LST_{anomaly}$). The integrated dataset (Dataset 3) was used to quantify immediate post-disturbance LST responses across Europe through statistical analysis and Random Forest modeling.

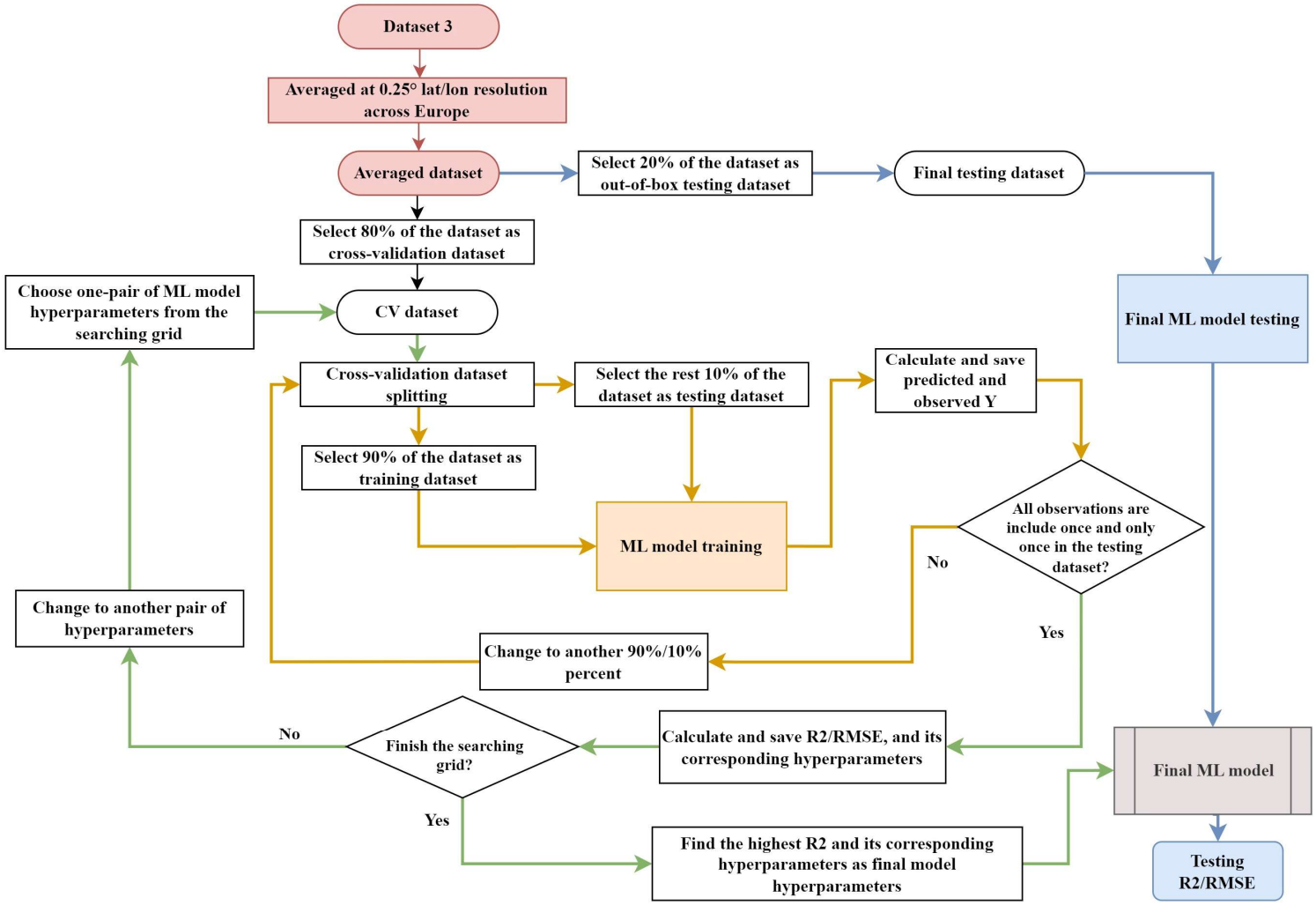

Supplementary Figure 3 | Random Forest (RF) model training, tuning, and testing workflow. Dataset 3 (instantaneous disturbance-induced LST anomalies) was aggregated to a 0.25° × 0.25° spatial resolution across Europe. The dataset was split into two parts: 80% for cross-validation (CV) and hyperparameter tuning, and 20% as an independent out-of-box (OOB) testing dataset. Within the CV dataset, repeated 10-fold splits (90% training, 10% testing) were used to train the RF model, iterating across a hyperparameter search grid. For each fold, model predictions were compared with observed values, and R^2 and RMSE were recorded. The best-performing hyperparameters were selected as the final RF model. This final model was then evaluated against the OOB testing dataset to ensure robust performance and generalization.

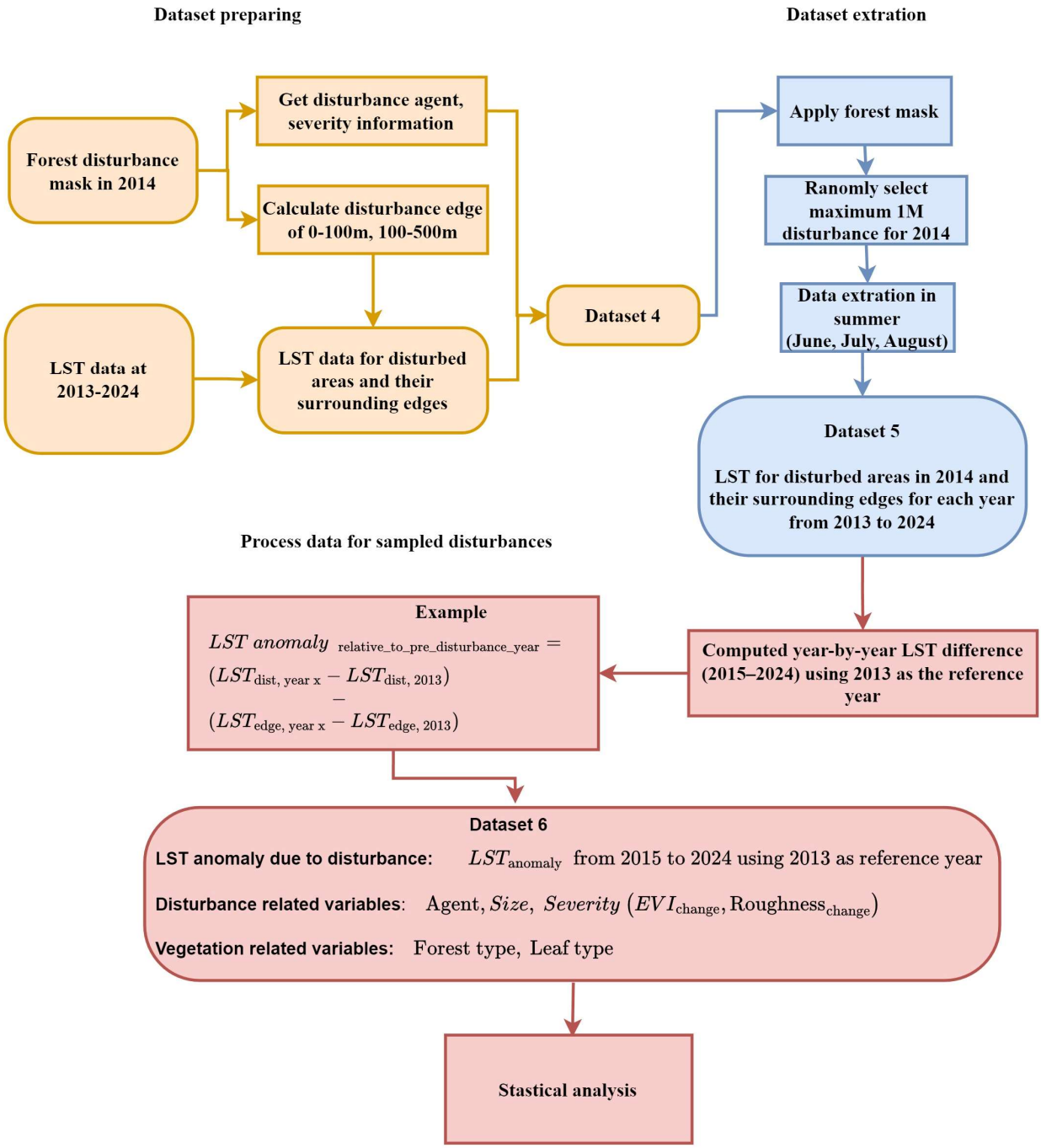

Supplementary Figure 4 | Workflow for analyzing post-disturbance LST recovery. Flowchart showing the preparation of disturbance and LST datasets, extraction of variables for disturbed areas and their forest edges, and calculation of recovery trajectories. Disturbances detected in 2014 were tracked annually from 2015 to 2024, with LST anomalies computed relative to the pre-disturbance baseline in 2013. The resulting integrated dataset (Dataset 6) includes disturbance attributes (agent, size, severity), Vegetation related variables (forest and leaf type), and was used to quantify recovery rates of disturbance-induced LST anomalies through statistical analysis.

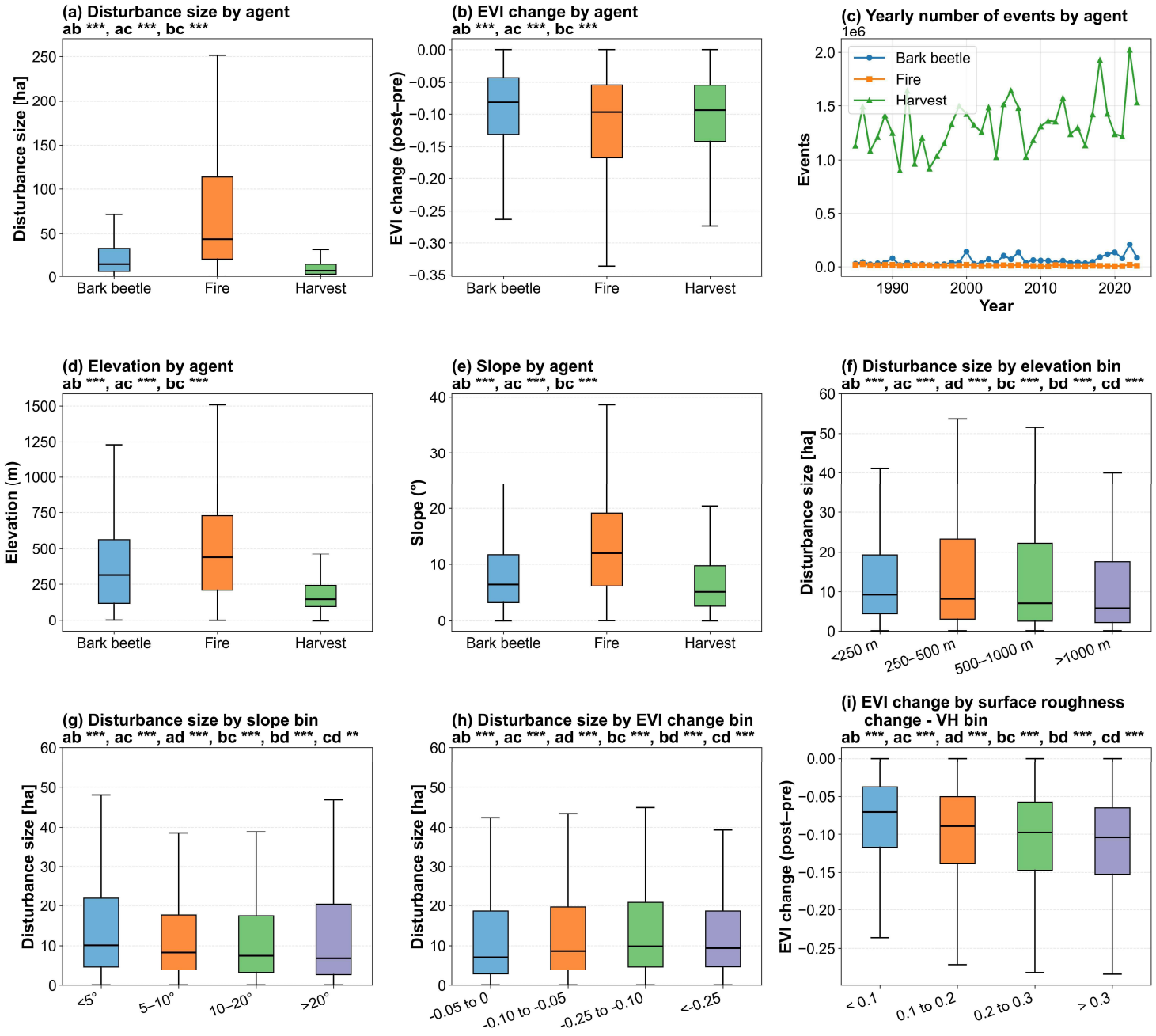

Supplementary Figure 5 | Disturbance, forest, and environmental attributes underlying spatial and agent-specific variability in post-disturbance LST responses across Europe. Panels (a)–(e) summarize the relationships between disturbance agent (bark beetle, fire, harvest) and disturbance size (a), severity (b, measured as EVI change), annual frequency (c), elevation (d), and slope (e) for all mapped events. Panel c shows time series of yearly event numbers by agent. Panels (f)–(i) explore how landscape and disturbance factors interact to shape patch size and severity: (f) disturbance size by elevation bin, (g) disturbance size by slope bin, (h) disturbance size by EVI change bin, and (i) EVI change (post–pre) by roughness change - VH bin. Patch size is plotted on a logarithmic scale in panels f–h. All boxplots show medians, interquartile ranges, and whiskers to 1.5× the interquartile range. Letters above the boxplots denote statistically distinct groups based on Kruskal–Wallis tests with post hoc pairwise comparisons (a, b, c, d indicate different groups; n.s., *, **, *** indicate $P > 0.05$, < 0.05, < 0.01, < 0.001).

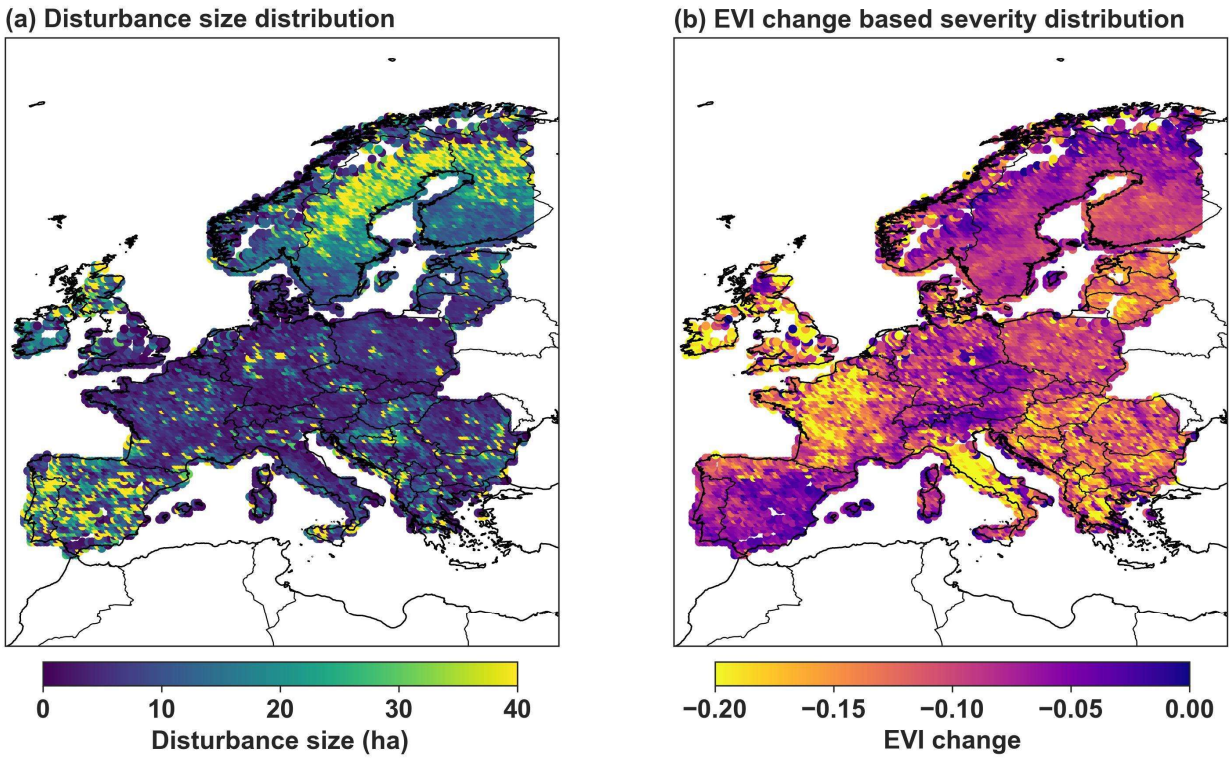

Supplementary Figure 6 | Spatial patterns of forest disturbance patch size and severity across Europe. Panel (a) shows the mean disturbance patch size (hectares) aggregated to a 0.25° × 0.25° grid for all mapped events, revealing a gradient from smaller disturbances in southern and central Europe to larger events in the north and east. Panel (b) maps the distribution of EVI change-based disturbance severity (post–pre), with darker red hues indicating stronger canopy loss and thus higher severity.

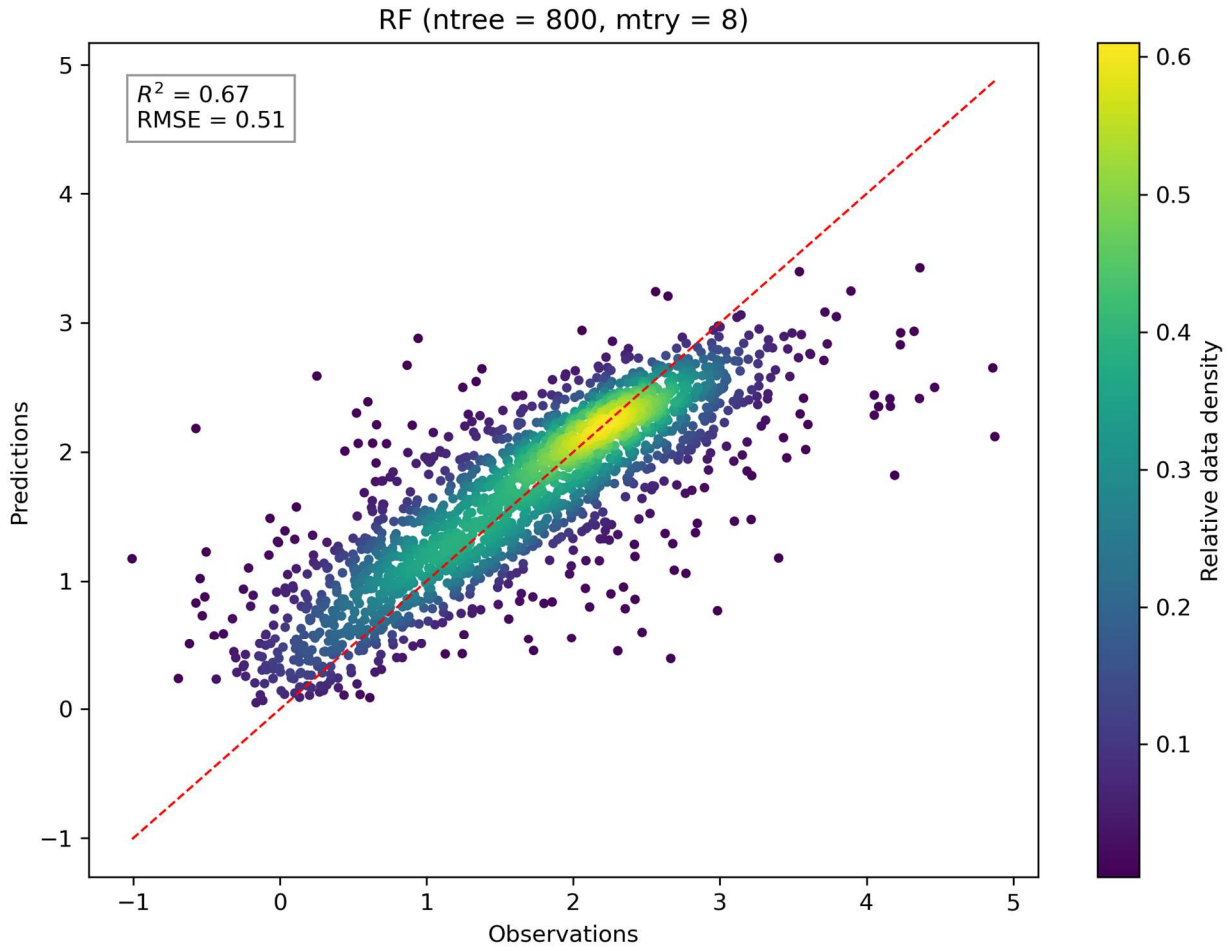

Supplementary Figure 7 | Performance of the Random Forest model for predicting disturbance-induced LST anomalies. Scatterplot comparing predicted versus observed LST anomalies (°C) across the independent testing dataset. The red dashed line represents the 1:1 reference line. The model achieved an R^2 of 0.67 and a root mean square error (RMSE) of 0.51, indicating moderate predictive skill. The background color scale shows the density of points, with warmer colors representing higher data density.

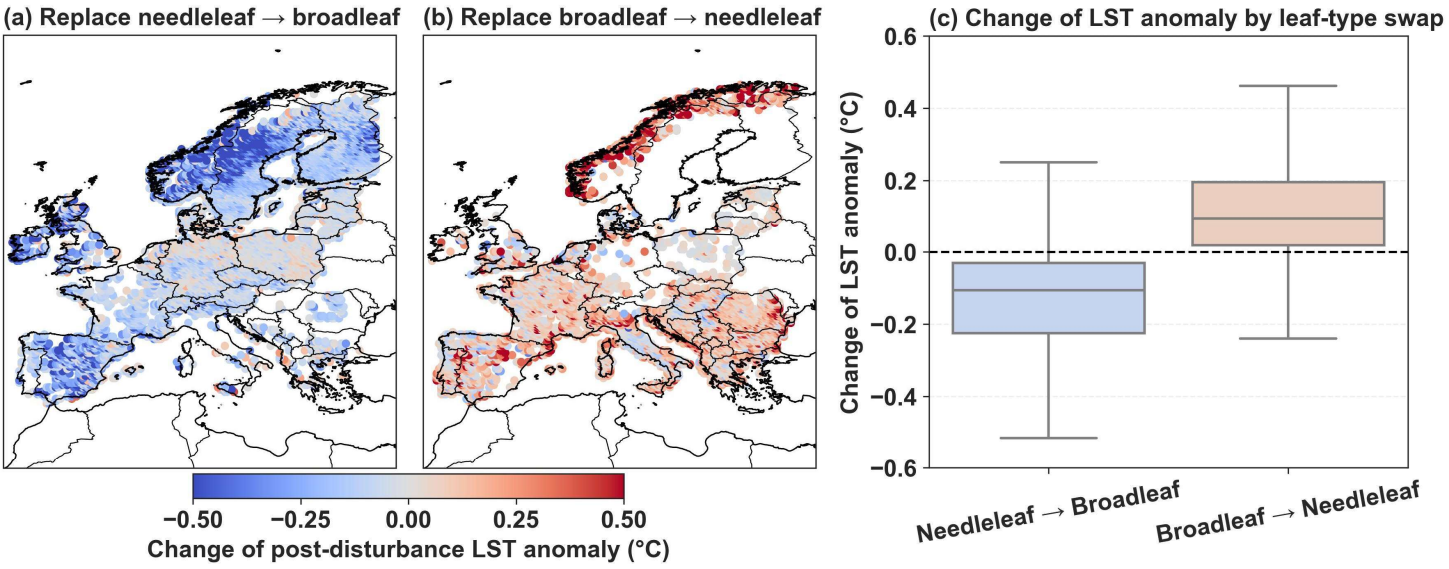

Supplementary Figure 8 | Effects of leaf-type transitions on post-disturbance LST across Europe. (a–b) Simulated changes in post-disturbance summer LST when dominant forest type is hypothetically converted from needleleaf → broadleaf (a) or broadleaf → needleleaf (b). Cooler (blue) and warmer (red) colors indicate reductions or increases, respectively, in LST anomalies of disturbed pixels relative to their 100–500 m adjacent undisturbed forest edges. Broadleaf replacement produces modest but spatially consistent cooling, strongest in Northern Europe, whereas the reverse transition yields weak and spatially heterogeneous warming. (c) Boxplots summarizing Europe-wide LST responses to leaf-type swaps. All simulations are derived from the random forest model trained on environmental, disturbance, and forest attributes aggregated at 0.25° × 0.25° spatial resolution. LST responses reflect predicted changes in post-disturbance thermal anomalies, defined as the difference between disturbed pixels and their adjacent undisturbed forest edges.

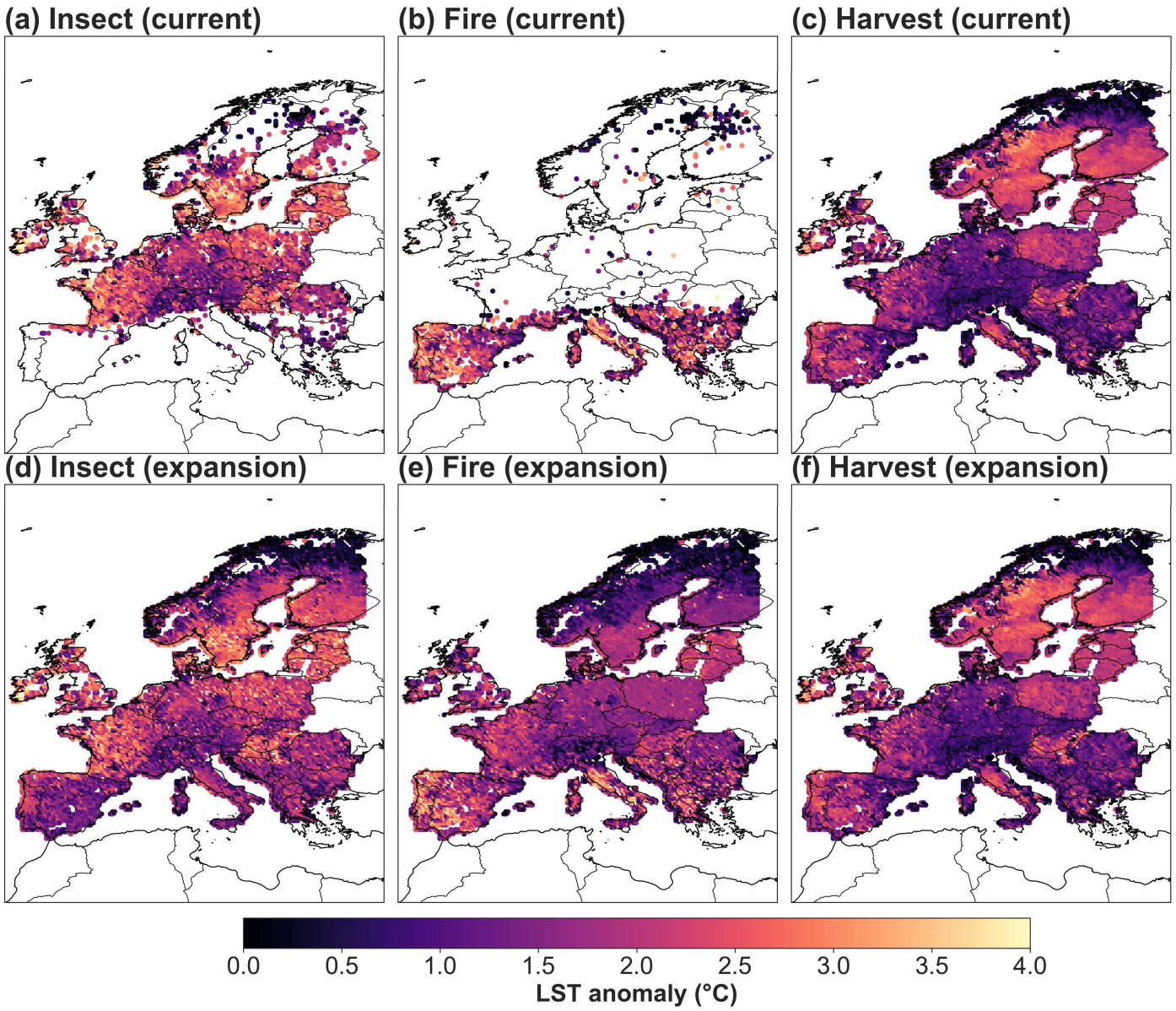

Supplementary Figure 9 | Current and potential future post-disturbance LST under expanded disturbance-agent ranges across Europe. Panel (a), Panel (b), and Panel (c) show the current post-disturbance summer LST anomalies for insect-, fire-, and harvest-driven disturbances, expressed as the difference between disturbed pixels and their adjacent undisturbed 100–500 m forest edges. Warm colors indicate stronger post-disturbance warming. Panel (d), Panel (e), and Panel (f) present simulated LST anomalies under a disturbance-expansion scenario in which each agent is allowed to occur across all forested regions (rather than being restricted to its contemporary ecological domain). These simulations use the random forest model trained on 0.25° × 0.25° aggregated environmental, forest, and disturbance attributes. Results show that expanding the geographic footprint of insect and fire disturbances shifts strong warming into regions that currently experience few such events, particularly northern and eastern Europe, while the widespread nature of harvest disturbances leads to comparatively similar warming patterns between current and expanded scenarios.

How historical-future patch-size evolution shape post-disturbance surface warming

We quantified historical changes in disturbance patch size across Europe by comparing the mean patch size within each 0.25° grid cell between 1989–1993 and 2019–2023 (**Supplementary figure 10a–c**). Assuming that these multi-decadal trends persist into the 2050s, we scaled pixel-level disturbance size accordingly and predicted the resulting LST response using the trained RF model. The model suggests that LST anomalies associated with insect outbreaks and fires are relatively insensitive to further size changes, likely because these disturbances already occur as large patches in many regions (**Supplementary figure 5a, Supplementary figure 10d, e, Figure 3f**). In contrast, harvesting disturbances show a stronger sensitivity to patch-size variation, with cooling under reduced patch sizes and additional warming under expanded patch sizes, consistent with the size-response patterns identified above. Importantly, harvesting activity has also intensified, with disturbance frequency increasing by ~1.5× over the past three decades and remaining substantially higher than that of the other two agents (**Supplementary figure 5c**). If these trends persist, the combined influence of increasingly frequent, larger, and more severe harvest disturbances could make forest management a disproportionately important driver of future local summertime surface warming across Europe.

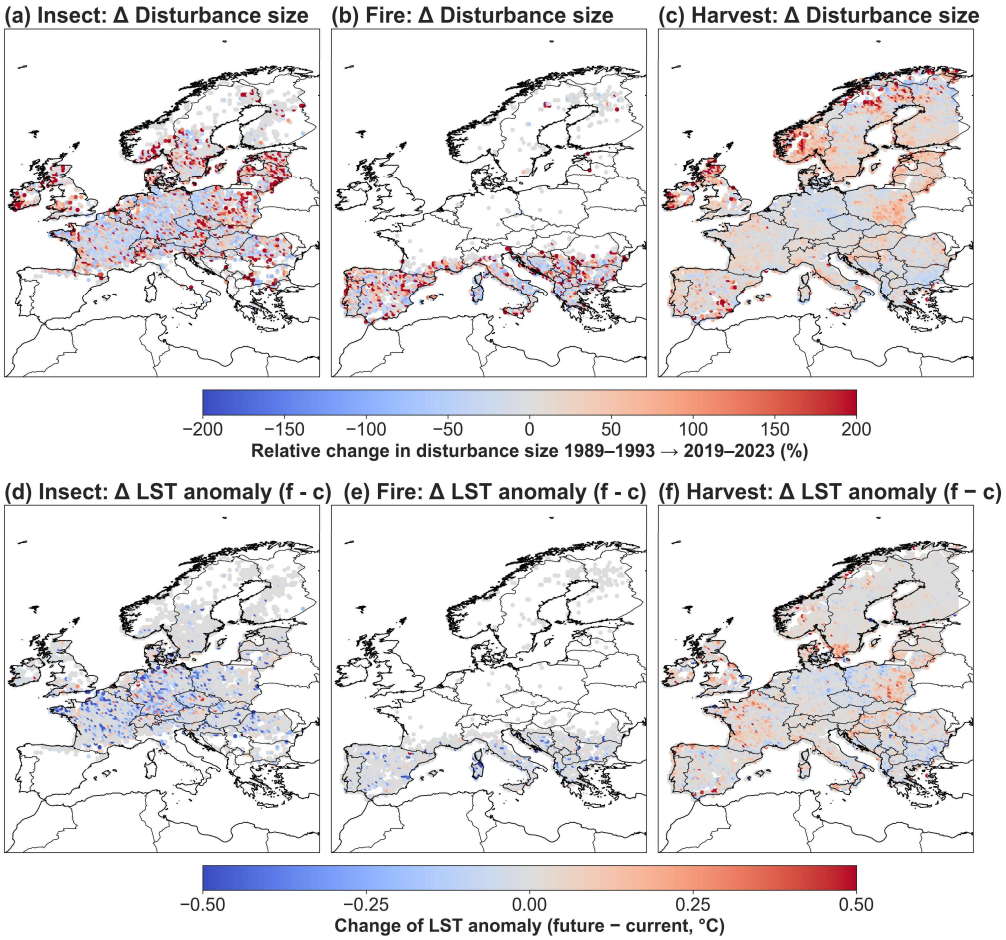

Supplementary figure 10 | Past-to-present shifts in disturbance size and their projected impact on post-disturbance LST across Europe. Panel (a), Panel (b), and Panel (c) show the relative change in mean disturbance patch size between 1989–1993 and 2019–2023 for insect outbreaks, fire, and harvesting,

aggregated to a 0.25° × 0.25° latitude–longitude grid. Red hues indicate an expansion of disturbance size, whereas blue hues indicate a contraction. Panel (d), Panel (e), and Panel (f) present the corresponding simulated changes in post-disturbance summer LST, expressed as the difference between future (2049–2053) and current (2019–2023) conditions, assuming that the past 30-year trend in patch-size change continues into the future. LST anomalies represent the difference between disturbed pixels and their adjacent undisturbed 100–500 m forest edges. Red areas denote enhanced future warming relative to today, while blue areas indicate reduced warming. Simulations are derived from the random forest model trained on environmental, disturbance, and forest structural attributes.

Tables

Supplementary table 1 | Random Forest model variables, definitions, and units

Category	Variable	Definition	Unit / Type
Response variable	**LST anomaly**	Summer LST difference between disturbed pixels and 100–500 m forest edges, before vs. after disturbance	°C
Disturbance characteristics	Disturbance size	Area of contiguous disturbed pixels within a year	ha (derived from 30 m pixels)
	Vegetation-index severity (EVI change)	Change in vegetation indices from pre- to post-disturbance; larger magnitude = stronger canopy loss	Unitless
	SAR roughness change (VV, VH)	Change in local standard deviation of Sentinel-1 backscatter in 5×5 kernel (post – pre disturbance) capturing structural disruption	dB
	Disturbance agent	Fire / wind–insect / harvest	Categorical
Forest structure and composition	Forest type	Primary / naturally regenerating / plantation	Categorical
	Leaf type	Broadleaf / needleleaf	Categorical
Vegetation state before disturbance	EVI	Mean pre-disturbance vegetation index values	Unitless
Surface structure before disturbance	Roughness_VV, Roughness_VH	Local standard deviation of Sentinel-1 backscatter in 5×5 kernel	dB
Environmental predictors	Elevation	Terrain height	m
	Slope	Local terrain slope	Degrees
	Sand (%)	Sand fraction of soil	%
	Clay (%)	Clay fraction of soil	%
	Latitude / Longitude	Geographic coordinates of 0.25° gridcell centroid	Degrees
Climate variables	Incoming radiation	Mean shortwave incoming radiation	W m^{-2}
	Near-surface (2m) air temperature	Mean summer air temperature at 2m height	°C
	Precipitation	Accumulated summer precipitation	mm

Supplementary table 2 | List of hyperparameters for Random Forest model

Hyperparameters	Values
Number of trees (ntree)	300, 500, 800, 1000
Number of random features (mtry)	3, 4, 5, …, number of total features